



JWST/NIRSpec Balmer-line Measurements of Star Formation and Dust Attenuation at $z \sim 3-6$

Alice E. Shapley¹ , Ryan L. Sanders^{2,7} , Naveen A. Reddy³ , Michael W. Topping⁴ , and Gabriel B. Brammer^{5,6}

¹ Department of Physics & Astronomy, University of California, Los Angeles, 430 Portola Plaza, Los Angeles, CA 90095, USA; aes@astro.ucla.edu

² Department of Physics and Astronomy, University of California, Davis, One Shields Avenue, Davis, CA 95616, USA

³ Department of Physics & Astronomy, University of California, Riverside, 900 University Avenue, Riverside, CA 92521, USA

⁴ Steward Observatory, University of Arizona, 933 N Cherry Avenue, Tucson, AZ 85721, USA

⁵ Cosmic Dawn Center (DAWN), Denmark

⁶ Niels Bohr Institute, University of Copenhagen, Lyngbyvej 2, DK-2100 Copenhagen Ø, Denmark

Received 2023 January 9; revised 2023 June 26; accepted 2023 July 21; published 2023 September 4

Abstract

We present an analysis of the star formation rates (SFRs) and dust attenuation properties of star-forming galaxies at $2.7 \leq z < 6.5$ drawn from the Cosmic Evolution Early Release Science Survey. Our analysis is based on JWST/NIRSpec Micro-Shutter Assembly $R \sim 1000$ spectroscopic observations covering approximately $1-5 \mu\text{m}$. Our primary rest-frame optical spectroscopic measurements are $\text{H}\alpha/\text{H}\beta$ Balmer decrements, which we use as an indicator of nebular dust attenuation. In turn, we use Balmer decrements to obtain dust-corrected $\text{H}\alpha$ -based SFRs (i.e., $\text{SFR}(\text{H}\alpha)$). We construct the relationship between $\text{SFR}(\text{H}\alpha)$ and stellar mass (M_*) in three bins of redshift ($2.7 \leq z < 4.0$, $4.0 \leq z < 5.0$, and $5.0 \leq z < 6.5$), which represents the first time the star-forming main sequence has been traced at these redshifts using direct spectroscopic measurements of Balmer emission as a proxy for SFR. In tracing the relationship between $\text{SFR}(\text{H}\alpha)$ and M_* back to such early times ($z > 3$), it is essential to use a conversion factor between $\text{H}\alpha$ and SFR that accounts for the subsolar metallicity prevalent among distant galaxies. We also use measured Balmer decrements to investigate the relationship between dust attenuation and stellar mass out to $z \sim 6$. The lack of significant redshift evolution in attenuation at fixed stellar mass, previously confirmed using Balmer decrements out to $z \sim 2.3$, appears to hold out to $z \sim 6.5$. Given the rapidly evolving gas, dust, and metal content of star-forming galaxies at fixed mass, this lack of significant evolution in attenuation provides an ongoing challenge to explain.

Unified Astronomy Thesaurus concepts: High-redshift galaxies (734); Galaxy evolution (594); Galaxy formation (595)

1. Introduction

Hydrogen Balmer-line emission from H II regions has long been recognized as one of the most robust probes of star formation and dust extinction in star-forming galaxies. The Balmer decrement based on the $\text{H}\alpha/\text{H}\beta$ flux ratio can be used to infer the amount of nebular attenuation, and, in turn, the dust-corrected, instantaneous star formation rate (SFR; e.g., Kennicutt 1998). The flux of a Balmer line, in combination with the UV continuum flux density, can also be used to infer the efficiency of ionizing photon production (e.g., Shivaie et al. 2018) and search for evidence of bursty past star formation histories (e.g., Domínguez et al. 2015; Guo et al. 2016; Emami et al. 2019; Atek et al. 2022).

Vast samples of galaxies with multiple Balmer emission-line measurements exist in the local Universe, from surveys such as the Sloan Digital Sky Survey (SDSS; Abazajian et al. 2009), and including both integrated spectra and spatially resolved emission-line maps (e.g., Belfiore et al. 2018; Ellison et al. 2018). Large samples of Balmer decrements and dust-corrected $\text{H}\alpha$ SFRs ($\text{SFR}(\text{H}\alpha)$) were assembled for the first time at $z > 1$ with the advent of the Hubble Space Telescope (HST)/WFC3

IR grism (Domínguez et al. 2013; Price et al. 2014; Battisti et al. 2022) as well as multi-object near-IR spectrographs on 8–10 m class ground-based telescopes (Reddy et al. 2015). These measurements were used to trace the so-called “main sequence” of galaxy formation during the epoch of peak SFR density in the Universe (Shivaie et al. 2015), constrain the nature of nebular dust attenuation and ISM geometry (Reddy et al. 2015, 2020; Shivaie et al. 2020), describe the spatially resolved growth of galaxy disks (Nelson et al. 2016), and investigate the relationship between dust attenuation and stellar mass (Shapley et al. 2022).

Until recently, it was impossible to perform such fundamental measures of the star-forming galaxy population past $z \sim 3$ because of both Earth’s atmosphere and a lack of the required instrumentation. Indeed, $\text{H}\alpha$ shifts past the red edge of the near-IR K band ($2.4 \mu\text{m}$) beyond a redshift of $z = 2.65$. The launch of JWST and the capabilities of its NIRSpec instrument (Ferruit et al. 2022) have transformed the ability to detect both $\text{H}\alpha$ and $\text{H}\beta$, respectively, out to $z \sim 6.5$ and $z \sim 9.3$. Recent NIRSpec observations from the Cosmic Evolution Early Release Science (CEERS) program (Finkelstein et al. 2022, 2023) showcase this ability beautifully, for the first time enabling Balmer decrement measurements based on $\text{H}\alpha$ and $\text{H}\beta$ fluxes for a large sample of galaxies at $z \sim 3-6$. Here we report on these Balmer decrements, as well as their implications for the SFRs ($\text{SFR}(\text{H}\alpha)$) and dust attenuation in typical star-forming galaxies extending from “cosmic noon” back into the reionization epoch.

⁷ NHFP Hubble Fellow.



Original content from this work may be used under the terms of the [Creative Commons Attribution 4.0 licence](https://creativecommons.org/licenses/by/4.0/). Any further distribution of this work must maintain attribution to the author(s) and the title of the work, journal citation and DOI.

In Section 2, we describe our observations, data reduction, measurements, and sample. In Section 3, we present results on the observed relationships between SFR($H\alpha$) and stellar mass, and Balmer decrement and stellar mass, measured for the first time at $z \sim 3$ –6. In Section 4, we consider the implications of these new measurements and consider future directions. Throughout, we adopt cosmological parameters of $H_0 = 70 \text{ km s}^{-1} \text{ Mpc}^{-1}$, $\Omega_m = 0.30$, and $\Omega_\Lambda = 0.7$ and a Chabrier (2003) initial mass function (IMF).

2. Observations and Sample

2.1. The CEERS NIRSpec Program

We use publicly available medium-resolution NIRSpec Micro-Shutter Assembly (MSA) data from the CEERS program (Program ID:1345; Finkelstein et al. 2022, 2023; P. Arrabal Haro et al., 2023, in preparation). The CEERS NIRSpec observations we analyzed consist of six pointings in the AEGIS field, all of which utilized the grating/filter combination of G140M/F100LP, G235M/F170LP, and G395M/F290LP, which provide a spectral resolution of $R \sim 1000$ over the wavelength range approximately 1 – $5 \mu\text{m}$. For each pointing, each grating/filter combination was observed for a total of 3107 s, broken down into three exposures of 14 groups, and adopting the NRSIRS2 readout mode. A three-point nod pattern was adopted for each observation, and each MSA “slit” consisted of three micro-shutters. Each of the six pointings contained between 52 and 55 targets, for a total sample of 321 slits and 318 distinct targets (three galaxies were observed on two pointings).

2.2. Data Reduction

We followed the same two-dimensional (2D) reduction procedures to reduce data for all three NIRSpec gratings. We began by passing individual uncalibrated detector images through the JWST `calwebb_detector1` pipeline.⁸ In this step, we masked all saturated pixels, subtracted the bias and dark current, and masked “snowballs” and “showers” associated with high-energy cosmic-ray events. Images were then corrected for striping by estimating and subtracting the $1/f$ noise in each image. We then cut out the 2D spectrum for each MSA slit and applied a flat-field correction, background subtraction using dithered exposures as the background, photometric calibration, and a wavelength solution based on the up-to-date calibration reference data system context (`jwst_1027.pmap`). Each slitlet was rectified and interpolated onto a common wavelength grid based on its grating and filter combination. Finally, individual calibrated 2D spectra exposures were combined following the defined three-shutter dither pattern, while excluding pixels that had been previously masked. The 2D error spectra represent a combination of the variance from Poisson noise, read noise, flat-fielding, and variance between exposures, summed in quadrature. This stage of the reduction yielded 310 targets with 2D spectra covering all three gratings, reflecting a negligible sample of eight initial targets that did not result in a viable 2D reduction.

One-dimensional (1D) science and error spectra were optimally extracted from the rectified 2D spectra (Horne 1986). The spatial profile in each grating was obtained by manually identifying wavelength ranges in the 2D spectrum containing

high signal-to-noise ratio (S/N) emission lines when present or detected continuum otherwise and summing the corresponding columns of the 2D spectrum. For targets with detected lines or continuum in at least one grating, a blind extraction was applied to any remaining grating lacking such information. Out of 310 CEERS targets with the full set of 2D spectra, we extracted 1D spectra for 252 (i.e., 81%). For the remaining 58 targets, in which we could identify neither lines nor continuum in any grating, we did not extract spectra, with either a manual or blind extraction technique.

As described in detail in Reddy et al. (2023), wavelength-dependent slit-loss corrections were estimated for each target based on its intrinsic morphology and position in the NIRSpec slit, as well as the wavelength-dependent JWST PSF. Intrinsic morphologies were estimated from JWST/NIRCam F115W imaging if available, or a Sérsic fit to HST/F160W imaging if not. In the absence of NIRCam F115W imaging or a robust Sérsic fit, a point source was assumed.

As described in detail in Sanders et al. (2023), the final flux calibration was achieved by scaling 1D science spectra to match the photometric spectral energy distributions (SEDs). Slit-loss-corrected NIRSpec spectra were passed through the available photometric filter transmission for each target to produce synthetic photometric flux densities and errors. The ratio of the image-based and synthetic flux densities was calculated for each filter in which both types of measurements had $S/N > 5$. If the number of filters meeting this requirement was ≥ 3 , 1D spectra and error spectra in all three gratings were scaled by the median of the individual ratios to achieve the final flux calibration. For the 109 targets that did not meet this criterion, no scale factor was applied. For the remaining 143 targets, the median scale factor was 0.997 with a standard deviation of 0.23 dex.

2.3. Measurements

Redshifts and emission-line fluxes were measured from the 1D spectra for which we were able to robustly identify emission lines. Reported redshifts for 231 galaxies are based on the best-fit centroid from a single Gaussian fit to the line with the highest S/N, usually $[\text{O III}]\lambda 5007$ (57%) or $H\alpha$ (36%). As described in more detail in Sanders et al. (2023), to estimate line fluxes, we used single Gaussian fits for widely separated lines; adjacent lines such as $[\text{N II}]\lambda 6548$, $H\alpha$, and $[\text{N II}]\lambda 6583$ are fit simultaneously with multiple Gaussians; and closely spaced lines that are blended and unresolved at $R \sim 1000$ are fit with a single Gaussian. The continuum model is taken to be the best-fit SED model (described in this section below), where the only free parameter is an additive offset. Using the best-fit SED model as the continuum has the advantage of self-consistently accounting for stellar absorption such that the measured hydrogen recombination line fluxes are robust.

The same emission line was measured in two adjacent gratings for many targets. These overlapping measurements showed good agreement, with a median offset of 0.02 dex and an intrinsic scatter of 0.08 dex for all emission lines detected at $\geq 3\sigma$ in both overlapping gratings, suggesting that the relative flux calibration between grating configurations is robust on average. In these cases of overlapping spectra, we adopted the inverse-variance weighted mean of the two available fluxes as our reported measurement.

⁸ <https://jwst-pipeline.readthedocs.io/en/latest/index.html>

We used existing multi-wavelength catalogs to derive best-fit SED models from which we infer stellar masses (M_*) and other stellar population parameters. Specifically, for the 99 CEERS NIRSpec targets with coverage, we used the publicly available catalog constructed by G. Brammer,⁹ which includes seven HST bands (F435W, F606W, F814W, F105W, F125W, F140W, and F160W) and seven JWST/NIRCam bands (F115W, F150W, F200W, F277W, F356W, F410M, and F444W) from the initial CEERS NIRCam observations in 2022 June. For an additional 185 objects we used the SEDs in the AEGIS field cataloged by the 3D-HST team (Skelton et al. 2014; Momcheva et al. 2016), which include ground-based and HST optical and near-IR photometry, and measurements from Spitzer/IRAC at 3.6–8.0 μm . There were 35 CEERS NIRSpec targets not covered by the Brammer HST+NIRCam catalog and lacking a robust multi-wavelength SED in the 3D-HST catalog. Restricted to the sample of 231 galaxies with NIRSpec spectroscopic redshifts, we found robust SED information for 210. When restricted to the redshift range forming the basis of this analysis, i.e., $2.7 \leq z \leq 6.5$, we have robust SEDs for 94 galaxies (an additional 15 galaxies with measured spectroscopic redshifts in this range lack SED information).

For SED modeling, we used the FAST program (Kriek et al. 2009), assuming the stellar population synthesis models of Conroy et al. (2009), and a Chabrier (2003) IMF. Following Reddy et al. (2018a), we adopted two combinations of metallicity and extinction curves for SED modeling. These include 1.4 solar metallicity ($Z_\odot = 0.014$) coupled with the Calzetti et al. (2000) attenuation curve (hereafter “1.4 Z_\odot + Calzetti”), and 0.27 solar models coupled with the Small Magellanic Cloud (SMC) extinction curve of Gordon et al. (2003; hereafter “0.27 Z_\odot + SMC”). We assumed delayed- τ star formation histories, where $\text{SFR}(t) \propto t \times \exp(-t/\tau)$. Here, t is the time since the onset of star formation and τ is the characteristic star formation timescale. The adoption of 1.4 Z_\odot + Calzetti or 0.27 Z_\odot + SMC was determined for each galaxy on the basis of its redshift and mass. Following Du et al. (2018) and guided by the evolving galaxy mass-metallicity relation (e.g., Sanders et al. 2021), at $z \leq 1.4$ we adopted 1.4 Z_\odot + Calzetti. At $1.4 < z \leq 2.7$ ($2.7 < z \leq 3.4$), we adopted 1.4 Z_\odot + Calzetti for galaxies above $\log(M_{*, 1.4Z_\odot + \text{Calzetti}}/M_\odot) = 10.45$ (10.66) and 0.27 Z_\odot + SMC for those at lower masses. At $z > 3.4$, we adopted 0.27 Z_\odot + SMC models (Reddy et al. 2018a) for all stellar masses. The choice of dust laws described above applies to the full CEERS NIRSpec spectroscopic sample. When restricted to the redshift range probed in the current analysis ($2.7 \leq z \leq 6.5$) and given the range of stellar masses spanned by such targets, all but one galaxy is modeled using 0.27 Z_\odot + SMC. We note that all relevant photometric bands were corrected for the contributions from strong nebular emission lines using the method described in Sanders et al. (2021), and Balmer emission-line fluxes were corrected for the underlying stellar absorption implied by the best-fit stellar population model.

Finally, $\text{SFR}(\text{H}\alpha)$ was estimated from dust-corrected $\text{H}\alpha$ luminosities. Reddy et al. (2020) showed that the Milky Way dust law of Cardelli et al. (1989) provides a good match to the wavelength dependence of nebular attenuation in $z \sim 2.3$ star-forming galaxies. Accordingly, we used the measured $\text{H}\alpha/\text{H}\beta$ ratio, along with an assumption of the Cardelli et al. (1989)

dust extinction curve, to infer $E(B - V)_{\text{neb}}$, the nebular extinction. Then the dust-corrected $\text{H}\alpha$ luminosity was multiplied by a conversion factor depending on the metallicity of the best-fit SED model. Given the subsolar metallicity prevalent among high-redshift galaxies (e.g., Cullen et al. 2019; Sanders et al. 2021), it is essential to use a conversion factor between $\text{H}\alpha$ and SFR that accounts for this property. Following the analysis of Reddy et al. (2018a), for galaxies with 1.4 Z_\odot + Calzetti fits, we used a conversion factor of $10^{-41.37} (M_\odot \text{ yr}^{-1}) / (\text{erg s}^{-1})$, derived from $Z = 0.02$ BPASS population synthesis models including the effects of stellar binaries and assuming an upper-mass IMF cutoff of $100 M_\odot$. This calibration is almost identical to the one from Hao et al. (2011) used in many other recent works for $\text{H}\alpha$ observations of $z \sim 2$ galaxies (Shivaei et al. 2015; Sanders et al. 2021; Shapley et al. 2022). For galaxies with 0.27 Z_\odot + SMC fits, we used a conversion factor of $10^{-41.67} (M_\odot \text{ yr}^{-1}) / (\text{erg s}^{-1})$, derived from $Z = 0.001$ BPASS population synthesis models including the effects of stellar binaries and assuming an upper-mass IMF cutoff of $100 M_\odot$ (Reddy et al. 2022). The latter lower conversion factor reflects the greater efficiency of ionizing photon production in lower-metallicity massive stars in binary systems.¹⁰

2.4. Sample

For the current analysis, we require a redshift measurement in the range $2.7 \leq z < 6.5$. The lower bound here represents the limit of ground-based measurements of $\text{H}\alpha$, i.e., the beginning of uncharted territory, while the upper bound represents the corresponding redshift limit imposed by the red cutoff of the G395M/F290LP setting. We also require a stellar-mass estimate, wavelength coverage of both $\text{H}\alpha$ and $\text{H}\beta$, a $\geq 3\sigma$ detection of $\text{H}\alpha$, and finally a lack of indication of active galactic nucleus (AGN) activity. In the full sample of CEERS spectra, we identified 15 galaxies as candidate AGN on the basis of either a $[\text{N II}]\lambda 6583/\text{H}\alpha$ ratio greater than 0.5 (10 galaxies) or else a $\text{H}\alpha$ profile consisting of both a narrow component and broad base (five galaxies).

Out of the 113 CEERS targets with redshifts measured at $2.7 \leq z < 6.5$ (Figure 1, left), 109 show no rest-optical spectroscopic evidence for AGN activity, of which 94 have stellar-mass estimates (Figure 1, right). Of these galaxies, 77 have (1) $\text{H}\alpha$ and $\text{H}\beta$ wavelength coverage and (2) $\text{H}\alpha$ detections, and they comprise our primary sample. This primary sample is plotted in all subsequent figures that show data points for individual galaxies and is representative of the larger sample of galaxies with measured redshifts in terms of redshift, stellar mass, and SFR as inferred from SED fitting. In order to search for evolution within the sample, we divide the primary sample into three redshift subsamples at $2.7 \leq z < 4$ (24 galaxies), $4.0 \leq z < 5.0$ (25 galaxies), and $5.0 \leq z < 6.5$ (28 galaxies). In what follows, we plot individual galaxies that have both detections and upper limits for $\text{H}\beta$. The 62 galaxies with $\text{H}\beta$ detections (81% of the primary sample) can be broken down into 22, 19, and 21 galaxies, respectively, at $2.7 \leq z < 4$, $4.0 \leq z < 5.0$, and $5.0 \leq z < 6.5$.

¹⁰ The stellar metallicity associated with this $\text{H}\alpha$ SFR conversion factor is lower than what is assumed for 0.27 Z_\odot + SMC broadband SED modeling, yet the conversion factor is not strongly metallicity dependent in this low-metallicity regime.

⁹ <https://s3.amazonaws.com/grizli-v2/JwstMosaics/v4/index.html>

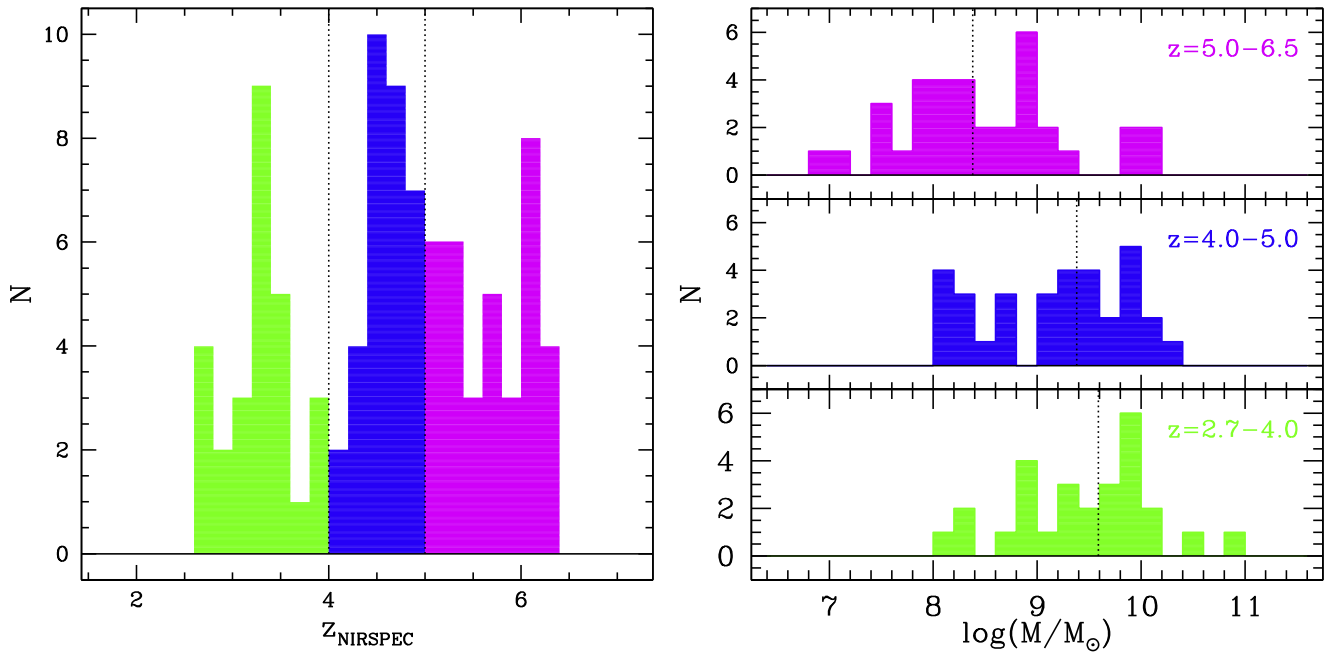


Figure 1. Left: redshift distribution of all 113 CEERS galaxies at $2.7 \leq z \leq 6.5$, from which the sample of star-forming galaxies we analyze is drawn. The three redshift bins we delineate are indicated in green ($2.7 \leq z < 4.0$), blue ($4.0 \leq z < 5.0$), and magenta ($5.0 \leq z < 6.5$). Right: stellar-mass distributions for the three redshift samples indicated in the left-hand panel, using the same color coding. For each redshift distribution, the median stellar mass is marked with a vertical dotted line. These median stellar-mass values are $\log(M_*/M_\odot) = 9.59, 9.38$, and 8.38 , respectively, for the $2.7 \leq z < 4.0$, $4.0 \leq z < 5.0$, and $5.0 \leq z < 6.5$ redshift samples.

3. Results

3.1. Star Formation

One of the key diagnostics of the evolution of the star-forming galaxy population across cosmic time is the so-called “main sequence” (e.g., Noeske et al. 2007). This correlation between SFR and M_* is thought to reflect the gradual growth of galaxies, largely through smooth accretion and minor mergers. A galaxy’s position with respect to the main sequence (within its scatter, significantly above, or significantly below), provides a sense of its evolutionary state.

In order to construct the SFR versus M_* relationship for CEERS galaxies targeted by NIRSpect, we took some care in translating dust-corrected $H\alpha$ luminosities. As described in Section 2.3, across the entire CEERS NIRSpect spectroscopic sample, the adopted conversion factor is lower for lower-mass and higher-redshift galaxies, based on the observed trend toward lower metallicity at lower stellar mass and higher redshift. In fact, in our primary sample, all but one galaxy was modeled with a subsolar metallicity and SMC dust law. Accordingly, we used the low-metallicity SFR/ $L_{H\alpha}$ conversion factor for all but one galaxy as well. We note that the sample median SFR($H\alpha$) estimated using this conversion factor shows excellent agreement (within 0.07 dex) with the median SFR derived from SED fitting (Section 2.3), and the two sets of SFR measurements are significantly correlated (see also Reddy et al. 2022).

Figure 2 shows the relationship between SFR($H\alpha$) and M_* among CEERS galaxies targeted by NIRSpect at $2.7 \leq z < 6.5$, color-coded by redshift range as in Figure 1. We also plot the best-fit parameterized main-sequence relation from Speagle et al. (2014), which expresses galaxy SFR as a function of both M_* and z or, equivalently, the age of the Universe. Relations from Speagle et al. (2014) are plotted at the median redshift of each of the three subsamples ($z = 3.30, 4.60$, and 5.65). Notably,

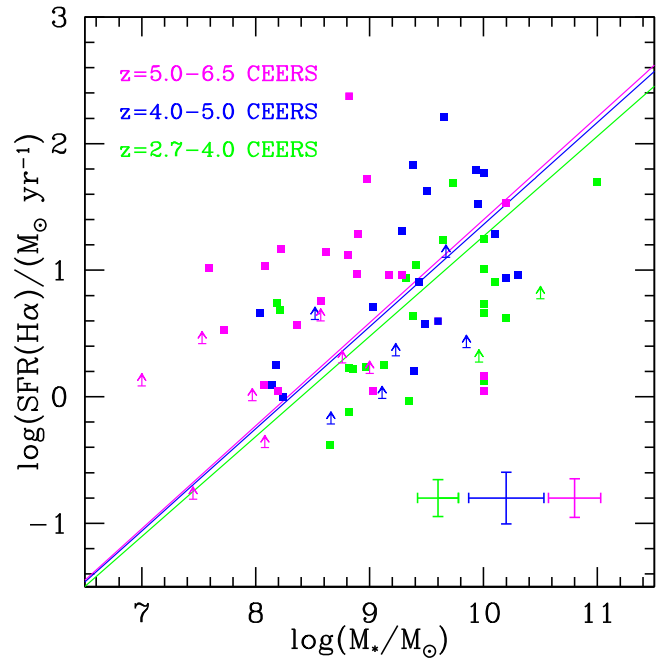


Figure 2. SFR($H\alpha$) vs. M_* . Green, blue, and magenta symbols are used, respectively, for the $2.7 \leq z < 4.0$, $4.0 \leq z < 5.0$, and $5.0 \leq z < 6.5$ samples, and galaxies with $H\beta$ upper limits are indicated as SFR($H\alpha$) lower limits (i.e., due to the lower limit on the Balmer decrement). The median error bar for each sample is shown in the lower right corner of the plot in its designated color. Along with CEERS data points, we plot the best-fit relation from Speagle et al. (2014; their Equation (28)) at the median redshift of each sample ($z = 3.30, 4.60$, and 5.65 , respectively, for the $2.7 \leq z < 4.0$, $4.0 \leq z < 5.0$, and $5.0 \leq z < 6.5$ samples) and offset by -0.34 dex in the y-axis to account for different assumptions regarding the conversion between observables and SFR.

we also shift the Speagle et al. (2014) relations by -0.34 dex in SFR($H\alpha$) since they are effectively tied to the Hao et al. (2011) SFR conversion factor for $H\alpha$.

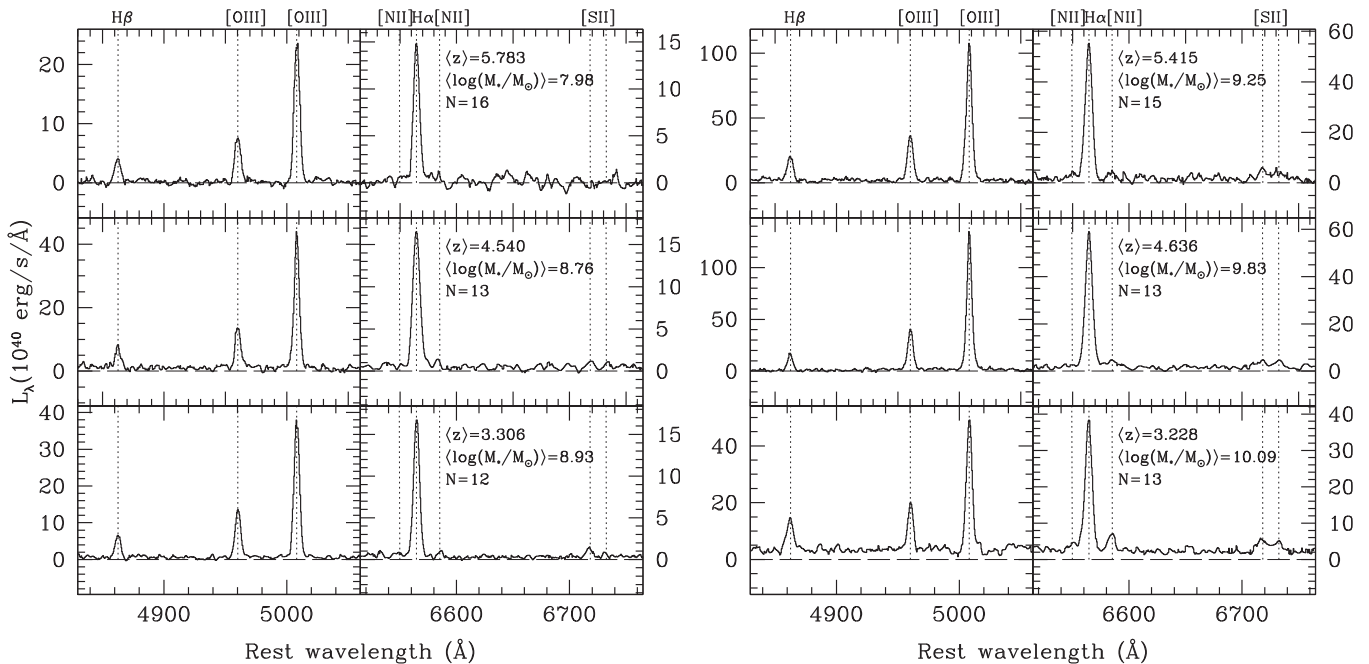


Figure 3. Composite spectra for each of the three redshift bins, where, from bottom to top, we show spectra, respectively, for the $2.7 \leq z < 4.0$, $4.0 \leq z < 5.0$, and $5.0 \leq z < 6.5$ samples. In each row, the left set of panels represents the “low-mass bin,” while the right side indicates the “high-mass bin,” where each redshift sample is divided at the median stellar mass. Each composite spectrum is zoomed in on the regions covering $H\beta$ and $[O\text{ III}]\lambda\lambda 4959, 5007$, as well as $H\alpha$, $[N\text{ II}]\lambda\lambda 6548, 6583$, and $[S\text{ II}]\lambda\lambda 6717, 6731$. These features are marked and labeled.

Both the $2.7 \leq z < 4.0$ and $4.0 \leq z < 5.0$ samples scatter symmetrically around the (shifted) main-sequence fits from Speagle et al. (2014), suggesting that these samples are representative of star-forming galaxies over the stellar-mass range $8.0 \leq \log(M_*/M_\odot) \leq 10.0$. The two lower-redshift subsamples also show no significant offset with respect to each other in terms of typical $\text{SFR}(H\alpha)$ at fixed M_* , consistent with the lack of strong redshift dependence in the Speagle et al. (2014) over this redshift range. The $5.0 \leq z < 6.5$ sample, however, is offset toward higher $\text{SFR}(H\alpha)$ relative to the Speagle et al. (2014) parameterization, which, itself, represents an extrapolation out to such high redshifts. Regardless of the parameterized version of the main sequence, the highest-redshift subsample is characterized by a higher average $\text{SFR}(H\alpha)$ at fixed stellar mass than the two lower-redshift subsamples within the stellar-mass range of overlap ($8.0 \leq \log(M_*/M_\odot) \leq 9.0$). More representative samples will be required to determine if this offset is reflective of the underlying evolving galaxy population, or rather a selection effect.

3.2. Dust Attenuation

It has been shown that the strong connection between measures of dust attenuation and M_* does not significantly evolve between $z \sim 0$ and $z \sim 2$. Here dust attenuation has been estimated with several different tracers, including the ratio of far-IR to UV SFRs or luminosities, also known as “IRX” (e.g., Meurer et al. 1999; Bouwens et al. 2016); the magnitude of far-UV (i.e., 1600 \AA) attenuation, or A_{1600} (e.g., McLure et al. 2018); the fraction of star formation that is obscured, f_{obscured} (Whitaker et al. 2017); and the nebular attenuation based on the Balmer decrement (i.e., $H\alpha/H\beta$ ratio; Domínguez et al. 2013; Kashino et al. 2013; Price et al. 2014). There is less consensus regarding the form of the attenuation versus M_* relation at

$z > 3$, with some evidence that it may evolve toward lower attenuation at fixed M_* (e.g., Fudamoto et al. 2020).

Shapley et al. (2022) presented a large sample of Balmer decrements at $z \sim 2.3$, demonstrating that the relationship between Balmer decrement and M_* showed no significant evolution up to the current epoch. We extend this work for the first time out to $z \sim 6.5$, using measured Balmer decrements for the CEERS NIRSspec sample. In addition to individual Balmer decrement measurements, we used stacked composite spectra to estimate average quantities in two bins of stellar mass for each of the three redshift bins. Composites were constructed by shifting the spectrum of each individual galaxy in a bin into the rest frame, converting from flux density to luminosity density, sampling each individual spectrum on a common wavelength grid, scaling each spectrum to match the average $H\alpha$ luminosity in the bin, and then averaging luminosity densities at each wavelength point using 3σ clipping. These composite spectra, zoomed in to the regions surrounding $H\beta$ and $H\alpha$, are shown in Figure 3. Each row features the results for one of the redshift subsamples, while the left-hand (right-hand) set of plots represents the lower-mass (higher-mass) half of each sample.¹¹

The left-hand panel of Figure 4 shows the relationship between Balmer decrement and M_* for both $z \sim 0$ star-forming galaxies in SDSS and $z \sim 2.3$ galaxies drawn from the MOSDEF survey (Shapley et al. 2022). We overplot individual CEERS NIRSspec measurements at $2.7 \leq z < 6.5$, color-coded by redshift subsample. The individual $z \geq 3$ measurements are noisy, but there is no obvious evolution between $z \sim 2.3$ and $z \sim 6.5$. With the assumption of the Cardelli et al. (1989) dust attenuation law, we can translate $H\alpha/H\beta$ to $E(B - V)_{\text{neb}}$ and

¹¹ The sample for stacking ($N = 82$) is slightly larger than for individual measurements as there was no explicit requirement of $H\beta$ coverage in the stacks.

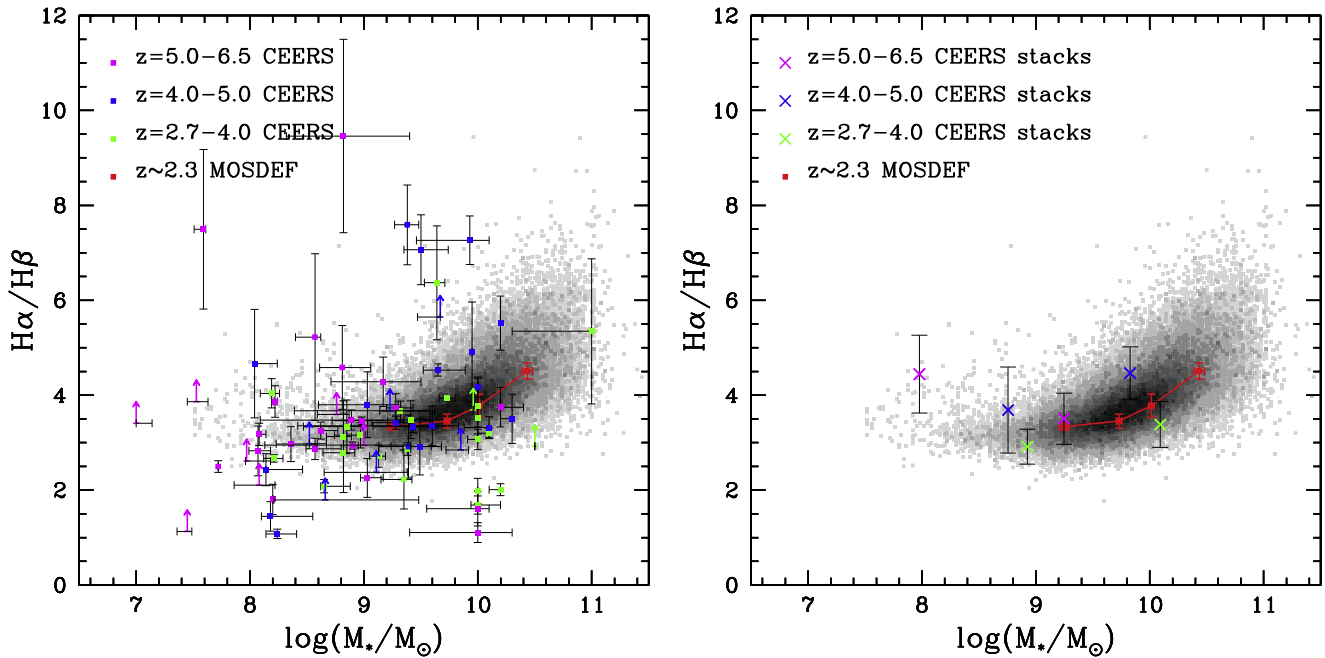


Figure 4. Attenuation vs. M_* based on the Balmer-line ratio, $H\alpha/H\beta$. In each panel, the background grayscale histogram corresponds to the distribution of local SDSS galaxies. The running median $H\alpha/H\beta$ ratio for $z \sim 2.3$ star-forming galaxies in the MOSDEF survey is shown in red (Shapley et al. 2022). In the left panel, we show individual CEERS galaxies color-coded by redshift as in previous plots. On the right, plotted $H\alpha/H\beta$ ratios are measured from composite spectra in two bins of stellar mass for each redshift range, as shown in Figure 3.

find that $E(B - V)_{\text{neb}}$ ranges from 0 to 1.19 in our $2.7 \leq z < 6.5$ sample, with a median of 0.18. We note that a small number of galaxies in the CEERS sample scatter to either surprisingly high values of $H\alpha/H\beta$ or else values significantly less than the dust-free minimum value of 2.79.¹² We attribute the majority of these outliers to remaining systematics in the NIRSpect grating-to-grating flux calibration (i.e., when $H\alpha$ and $H\beta$ are measured in different gratings), which lacks bias on average but also has scatter.

In the right-hand panel of Figure 4, we replace individual CEERS measurements with those taken from composite spectra. In these higher-S/N measurements, the two lower-redshift samples show preliminary evidence for higher $H\alpha/H\beta$ ratio at higher stellar mass, yet the error bars are still too large to discern a significant trend. Furthermore, at lower redshifts, only a very shallow trend between $H\alpha/H\beta$ and stellar mass is observed over the stellar-mass range probed by the $z > 3$ sample. The main result from these preliminary measurements of dust attenuation and stellar mass in CEERS is that the $z > 3$ measurements scatter around those at $z \sim 0-2.3$, with no obvious offset overall. We do note that the lower-mass bin at $5.0 \leq z < 6.5$ is offset toward higher $H\alpha/H\beta$ relative to the SDSS distribution (there are no $z \sim 2.3$ measurements at $\log(M_*/M_\odot) \sim 8.0$), but the error bar for this 16-galaxy stack is large enough that its vertical offset relative to SDSS is not significant, and the lower- and higher-mass bins at this redshift are statistically consistent with a flat trend.

4. Discussion

A crucial component of our measurement of the $\text{SFR}(H\alpha)$ versus M_* relation at $2.7 \leq z < 6.5$ is the adoption of an appropriate conversion factor between dust-corrected $H\alpha$ luminosity and SFR, characterized by the correct metallicity and treatment of the effects of stellar binaries. There are multiple lines of evidence that the vast majority of galaxies in our sample have significantly subsolar metallicities. Their stellar masses alone suggest subsolar metallicity, given what is known about the evolution of the galaxy mass–metallicity relation at lower redshifts (e.g., Sanders et al. 2021). For example, given the median stellar mass of our primary $2.7 \leq z < 6.5$ sample (i.e., $\log(M_*/M_\odot) = 9.11$), the corresponding oxygen abundance in the $z \sim 3.3$ mass–metallicity relationship of Sanders et al. (2021) is $12 + \log(\text{O}/\text{H}) = 8.15$ (i.e., 0.28 solar). Assuming that the mass–metallicity relationship evolves toward lower metallicity at fixed mass as redshift increases (e.g., Torrey et al. 2019), we regard this metallicity as an upper limit for the typical value characterizing our primary sample. More directly, as discussed in Shapley et al. (2023), the composite spectra shown in Figure 3 indicate $[\text{N II}]/\text{H} \alpha \leq 0.1$ for all subsamples, another sign of low metallicity (Pettini & Pagel 2004). Finally, models of the rest-UV stellar continuum of $z \sim 2-3$ star-forming galaxies suggests significantly subsolar stellar metallicities (Steidel et al. 2016; Cullen et al. 2019; Topping et al. 2020a, 2020b; Reddy et al. 2022). Star-forming galaxies such as those in the CEERS NIRSpect sample, covering the same or lower stellar-mass range but at higher redshift, should be even less enriched. As highlighted by Reddy et al. (2018b) and Theios et al. (2019), the subsolar conversion factor between $H\alpha$ luminosity and SFR adopted here is a factor of ~ 2.5 lower than the canonical conversion used for lower-redshift studies in the literature (e.g., Hao et al. 2011). Previously, Caputi et al. (2017) estimated the $\text{SFR}(H\alpha)$ versus M_* relation at $z \sim 4-5$, based on a large

¹² We adopt an intrinsic ratio of 2.79 for $H\alpha/H\beta$, which is based on assuming an electron temperature of $T_e = 15000$ K. This temperature is typical of high-redshift, subsolar-metallicity star-forming galaxies (Sanders et al. 2020, 2023; Reddy et al. 2022; Curti et al. 2023).

sample of star-forming galaxies with photometric redshifts and $H\alpha$ line fluxes inferred indirectly from Spitzer/IRAC $3.6\ \mu\text{m}$ photometric excesses relative to best-fit SED models. Caputi et al. (2017) used a solar-metallicity conversion factor for $\text{SFR}(H\alpha)$, resulting in a higher overall normalization of the $\text{SFR}(H\alpha)$ versus M_* relation, and also found an apparent bimodality in the SFRs of galaxies with strong $H\alpha$ emission. We recover no such bimodality in the distribution of $\text{SFR}(H\alpha)$ values, based on direct spectroscopic measurements of Balmer lines.

The CEERS NIRSpec sample provides tantalizing evidence that the relationship between Balmer decrement and stellar mass remains constant out to $z \sim 6.5$. This measure of dust attenuation depends on both the dust mass and the way in which it is distributed (i.e., the effective dust-mass surface density), so the lack of evolution in attenuation at fixed stellar mass suggests a constant ratio of dust-mass surface density to stellar mass (Shapley et al. 2022). At the same time, other studies have found evidence for a lower fraction of obscured star formation (“IRX”) at fixed mass at $z > 4$ (e.g., Fudamoto et al. 2020), based on far-IR and UV continuum estimate of dust attenuation. Different redshift evolution in the IRX versus M_* and $H\alpha/H\beta$ versus M_* relations could arise if the spatial distribution of dust relative to massive stars and H II regions evolves (Reddy et al. 2015), based on the fact that IRX probes stellar continuum attenuation while $H\alpha/H\beta$ traces nebular attenuation in H II regions. However, the results thus far on the attenuation versus mass relation at the highest redshifts—both our Balmer decrement analysis and the studies based on IRX—use small samples of galaxies and require confirmation with an order of magnitude larger sample numbers.

We have entered an era in which spectroscopic Balmer-line measurements at $z > 3$ are routine and can be obtained in modest exposure times on JWST. The CEERS NIRSpec data set analyzed here demonstrates the great potential of JWST for obtaining fundamental probes of the star-forming galaxy population into the reionization epoch based on Balmer-line measurements. In addition to tracing star formation, galaxy growth, and dust attenuation, as we do here, the ratio of $H\alpha$ to UV continuum luminosity can be used to infer the efficiency of ionizing photon production, ξ_{ion} (Shivaei et al. 2018)—crucial for quantifying the role of star-forming galaxies in cosmic reionization—as well as evidence for bursty star formation histories (Emami et al. 2019). To fully utilize Balmer-line ratios at $z > 3$ and robustly infer dust-corrected SFRs and other key galaxy properties, we must limit wavelength-dependent systematic uncertainties in NIRSpec flux calibration. We look forward to realizing the full potential of JWST and NIRSpec with not only larger and representative galaxy samples, but also samples with complete NIRCам photometric coverage, selected from early public JWST imaging data sets.

Acknowledgments

We acknowledge the entire CEERS team for their effort to design and execute this Early Release Science observational program, especially the work to design the MSA observations. This work is based on observations made with the NASA/ESA/CSA James Webb Space Telescope. The data were obtained from the Mikulski Archive for Space Telescopes at the Space Telescope Science Institute, which is operated by the Association of Universities for Research in Astronomy, Inc.,

under NASA contract NAS5-03127 for JWST. The specific observations analyzed can be accessed via doi:10.17909/z7p0-8481. We also acknowledge support from NASA grant JWST-GO-01914. Support for this work was also provided through the NASA Hubble Fellowship grant #HST-HF2-51469.001-A awarded by the Space Telescope Science Institute, which is operated by the Association of Universities for Research in Astronomy, Incorporated, under NASA contract NAS5-26555.

ORCID iDs

Alice E. Shapley  <https://orcid.org/0000-0003-3509-4855>
 Ryan L. Sanders  <https://orcid.org/0000-0003-4792-9119>
 Naveen A. Reddy  <https://orcid.org/0000-0001-9687-4973>
 Michael W. Topping  <https://orcid.org/0000-0001-8426-1141>
 Gabriel B. Brammer  <https://orcid.org/0000-0003-2680-005X>

References

- Abazajian, K. N., Adelman-McCarthy, J. K., Agüeros, M. A., et al. 2009, *ApJS*, **182**, 543
- Atek, H., Furtak, L. J., Oesch, P., et al. 2022, *MNRAS*, **511**, 4464
- Battisti, A. J., Bagley, M. B., Baronchelli, I., et al. 2022, *MNRAS*, **513**, 4431
- Belfiore, F., Maiolino, R., Bundy, K., et al. 2018, *MNRAS*, **477**, 3014
- Bouwens, R. J., Aravena, M., Decarli, R., et al. 2016, *ApJ*, **833**, 72
- Calzetti, D., Armus, L., Bohlin, R. C., et al. 2000, *ApJ*, **533**, 682
- Caputi, K. I., Deshmukh, S., Ashby, M. L. N., et al. 2017, *ApJ*, **849**, 45
- Cardelli, J. A., Clayton, G. C., & Mathis, J. S. 1989, *ApJ*, **345**, 245
- Chabrier, G. 2003, *PASP*, **115**, 763
- Conroy, C., Gunn, J. E., & White, M. 2009, *ApJ*, **699**, 486
- Cullen, F., McLure, R. J., Dunlop, J. S., et al. 2019, *MNRAS*, **487**, 2038
- Curti, M., D’Eugenio, F., Camiani, S., et al. 2023, *MNRAS*, **518**, 425
- Domínguez, A., Siana, B., Brooks, A. M., et al. 2015, *MNRAS*, **451**, 839
- Domínguez, A., Siana, B., Henry, A. L., et al. 2013, *ApJ*, **763**, 145
- Du, X., Shapley, A. E., Reddy, N. A., et al. 2018, *ApJ*, **860**, 75
- Ellison, S. L., Sánchez, S. F., Ibarra-Medel, H., et al. 2018, *MNRAS*, **474**, 2039
- Emami, N., Siana, B., Weisz, D. R., et al. 2019, *ApJ*, **881**, 71
- Ferruit, P., Jakobsen, P., Giardino, G., et al. 2022, *A&A*, **661**, A81
- Finkelstein, S. L., Bagley, M. B., Ferguson, H. C., et al. 2023, *ApJL*, **946**, L13
- Finkelstein, S. L., Bagley, M. B., Haro, P. A., et al. 2022, *ApJL*, **940**, L55
- Fudamoto, Y., Oesch, P. A., Magnelli, B., et al. 2020, *MNRAS*, **491**, 4724
- Gordon, K. D., Clayton, G. C., Misselt, K. A., Landolt, A. U., & Wolff, M. J. 2003, *ApJ*, **594**, 279
- Guo, Y., Rafelski, M., Faber, S. M., et al. 2016, *ApJ*, **833**, 37
- Hao, C.-N., Kennicutt, R. C., Johnson, B. D., et al. 2011, *ApJ*, **741**, 124
- Horne, K. 1986, *PASP*, **98**, 609
- Kashino, D., Silverman, J. D., Rodighiero, G., et al. 2013, *ApJL*, **777**, L8
- Kennicutt, R. C., Jr. 1998, *ARA&A*, **36**, 189
- Kriek, M., van Dokkum, P. G., Labbé, I., et al. 2009, *ApJ*, **700**, 221
- McLure, R. J., Dunlop, J. S., Cullen, F., et al. 2018, *MNRAS*, **476**, 3991
- Meurer, G. R., Heckman, T. M., & Calzetti, D. 1999, *ApJ*, **521**, 64
- Momcheva, I. G., Brammer, G. B., van Dokkum, P. G., et al. 2016, *ApJS*, **225**, 27
- Nelson, E. J., van Dokkum, P. G., Momcheva, I. G., et al. 2016, *ApJL*, **817**, L9
- Noeske, K. G., Weiner, B. J., Faber, S. M., et al. 2007, *ApJL*, **660**, L43
- Pettini, M., & Pagel, B. E. J. 2004, *MNRAS*, **348**, L59
- Price, S. H., Kriek, M., Brammer, G. B., et al. 2014, *ApJ*, **788**, 86
- Reddy, N. A., Kriek, M., Shapley, A. E., et al. 2015, *ApJ*, **806**, 259
- Reddy, N. A., Oesch, P. A., Bouwens, R. J., et al. 2018a, *ApJ*, **853**, 56
- Reddy, N. A., Shapley, A. E., Kriek, M., et al. 2020, *ApJ*, **902**, 123
- Reddy, N. A., Shapley, A. E., Sanders, R. L., et al. 2018b, *ApJ*, **869**, 92
- Reddy, N. A., Topping, M. W., Sanders, R. L., Shapley, A. E., & Brammer, G. 2023, *ApJ*, **948**, 83
- Reddy, N. A., Topping, M. W., Shapley, A. E., et al. 2022, *ApJ*, **926**, 31
- Sanders, R. L., Shapley, A. E., Jones, T., et al. 2021, *ApJ*, **914**, 19
- Sanders, R. L., Shapley, A. E., Reddy, N. A., et al. 2020, *MNRAS*, **491**, 1427
- Sanders, R. L., Shapley, A. E., Topping, M. W., Reddy, N. A., & Brammer, G. B. 2023, arXiv:2301.06696

- Shapley, A. E., Reddy, N. A., Sanders, R. L., Topping, M. W., & Brammer, G. B. 2023, [ApJL](#), **950**, L1
- Shapley, A. E., Sanders, R. L., Salim, S., et al. 2022, [ApJ](#), **926**, 145
- Shivaei, I., Reddy, N., Rieke, G., et al. 2020, [ApJ](#), **899**, 117
- Shivaei, I., Reddy, N. A., Shapley, A. E., et al. 2015, [ApJ](#), **815**, 98
- Shivaei, I., Reddy, N. A., Siana, B., et al. 2018, [ApJ](#), **855**, 42
- Skelton, R. E., Whitaker, K. E., Momcheva, I. G., et al. 2014, [ApJS](#), **214**, 24
- Speagle, J. S., Steinhardt, C. L., Capak, P. L., & Silverman, J. D. 2014, [ApJS](#), **214**, 15
- Steidel, C. C., Strom, A. L., Pettini, M., et al. 2016, [ApJ](#), **826**, 159
- Theios, R. L., Steidel, C. C., Strom, A. L., et al. 2019, [ApJ](#), **871**, 128
- Topping, M. W., Shapley, A. E., Reddy, N. A., et al. 2020a, [MNRAS](#), **499**, 1652
- Topping, M. W., Shapley, A. E., Reddy, N. A., et al. 2020b, [MNRAS](#), **495**, 4430
- Torrey, P., Vogelsberger, M., Marinacci, F., et al. 2019, [MNRAS](#), **484**, 5587
- Whitaker, K. E., Pope, A., Cybulski, R., et al. 2017, [ApJ](#), **850**, 208